Analysis and Suppression of Circulating Current Caused by Carrier Phase Difference in Parallel Voltage Source Inverters With SVPWM

Zhang Xueguang, *Member, IEEE*, Weiwei Li, Yi Xiao, Gaolin Wang, *Member, IEEE*, and Dianguo Xu, *Fellow, IEEE*

***Abstract*—Although high-frequency circulating current exists in parallel-operated inverters, it has not attracted as much attention as low-frequency circulating current, and thus has not been analyzed in detail previously. In this paper, a mathematical model and analysis are presented, which reveal the spectrum components and their changing trends of the circulating currents caused by carrier phase differences. The impact of carrier phase difference on high-frequency circulating current is also analyzed and verified. A closed-loop control scheme is proposed to suppress the switching frequency circulating current caused by carrier phase difference. In addition, the deadbeat and closed-loop control are combined to suppress the low- and high-frequency circulating currents simultaneously, to improve the overall performance of circulating current suppression. The effectiveness of the proposed scheme is verified by the simulation and experimental results acquired from a laboratory platform.**

***Index Terms*—Carrier phase difference, circulating current control, parallel voltage source inverters, switching frequency circulating current.**

I. Introduction

With the increase in converter capacity in wind power and PV industries, it is common to provide parallel power modules to ensure higher power ratings, redundancy, reliability, and flexibility, along with several other advantages such as smaller switching stress, lower cost, and lower maintenance [1]–[3]. Research efforts focus on parallel inverters including power sharing and circulating current suppression. For power- or load-current sharing [4], [5], parallel-operated inverters could have different hardware topologies, circuit parameters, modulation techniques, and controller parameters, because they are

Manuscript received January 3, 2018; revised March 12, 2018; accepted April 4, 2018. Date of publication April 12, 2018; date of current version September 28, 2018. This work was supported by the National Key Research and Development Program of China under Grant 2018YFB0904000, and the National Natural Science Foundation of China under Grant 51577040 and Grant 51720105008. Recommended for publication by Associate Editor A. M. Trzynadlowski. *(Corresponding author: Zhang Xueguang.)*

Z. Xueguang, W. Li, Y. Xiao and D. Xu are with the Department of Electrical Engineering, Harbin Institute of Technology, Harbin 150001, China (e-mail:

The previous works mentioned above mostly focus on the low-frequency ZSCC, which occurs when the average ZSV generated by the parallel inverter modules is different. The difference in ZSV may be caused by inconsistent modulation signals or small discrepancies in the hardware parameters, controller parameters, and reference currents under practical conditions.

In comparison, the high-frequency ZSCC in parallel-operated inverters does not attract as much attention as its low-frequency counterpart, and has not been analyzed in detail previously. Asynchronous carriers will cause high-frequency ZSCCs, accompanied by low-frequency envelopes; further, it is easily conceivable that carrier synchronization can be applied to solve the problem. However, it is relatively difficult to synchronize carriers between parallel modules with independent controllers and without communications. Liu *et al.* [31] proposed a method to restrain circulating current by carrier phase difference adjustment, but it requires the hardware parameters of parallel modules to be identical, which is rarely satisfied in practical hardware platforms. Liu *et al.* [32] illustrated the relationship between high-frequency ZSCC and carrier phase difference. However, the phase difference is limited within a small range, and the analysis results need to be further proved by simulations and experiments. Jiang *et al.* [33] proposed a useful method to synchronize carriers between modules, but it is only valid without the injection of ZSV, therefore it is not suitable for SVM and the dc voltage utilization is limited. Furthermore, a virtual oscillator is implemented to synchronize carrier waves between parallel inverters, but additional passive components are required, and the controller design is complicated [34].

The primary contribution of this paper consists of the following three points.

1) Although it is well known that the carrier phase difference in a parallel inverter system will produce high-frequency circulation currents, many aspects still need to be studied, e.g., the specific relationship between circulating current and carrier phase difference, the spectrum components of the high-frequency circulating current, and how the circulating current changes with respect to different carrier phase differences. Therefore, this study will focus on the characteristics of the circulating current caused by carrier phase difference, which have not been discussed in previous literatures. Compared to the limited range of the carrier phase difference in [32], this study considers the full range. Liu *et al.* [32] and [33] are only suitable for sinusoidal pulsewidth modulation (SPWM), while this study handles SVM that has higher dc voltage utilization.
2) All the mathematical model and spectrum analysis are proven by simulation and experimental results. The circulating current and its spectrum with respect to different carrier phase differences are provided, to verify the relationship between the circulating current and the carrier phase difference.
3) A closed-loop carrier phase controller is proposed to suppress the switching-frequency circulating current caused by the carrier phase difference, and subsequently combined with deadbeat control to restrain the low-frequency circulating current, to achieve better overall suppressing performance. As the high-frequency and low-frequency components of the circulating current are difficult to be dealt simultaneously, they are typically studied separately in previous works. However, this study attempts to suppress the high- and low-frequency circulating currents simultaneously.

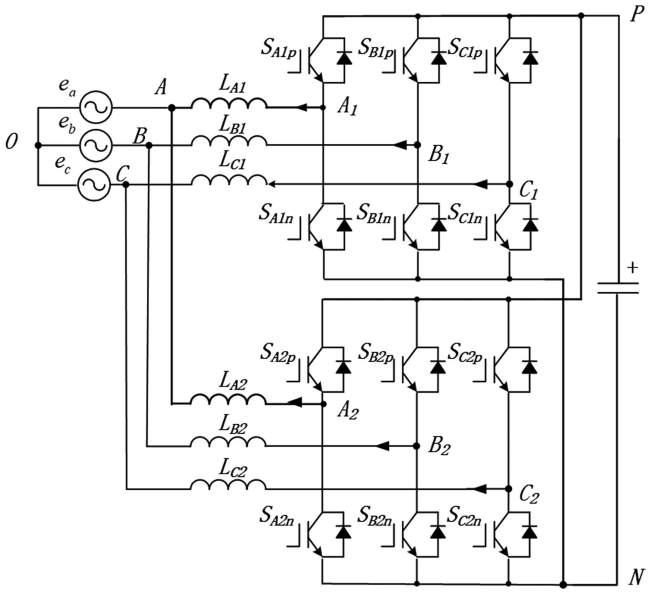

Fig. 1. Topology of a parallel inverter system.

This paper is organized as follows. Section II introduces some of the fundamentals and definitions of circulating current in parallel-operated inverters. Section III deduces the mathematical expression of the circulating current caused by carrier phase difference, and then analyzes the components and characteristics of the circulating current. Based on the mathematical model and theoretical analysis, a closed-loop control scheme is proposed to adjust the carrier phase difference between the parallel modules to restrain the circulating current. The simulation and experimental results are provided in Section IV. Finally, the conclusion of this paper is presented in Section V.

II. Circulating Current in Parallel Voltage Source Inverters

The topology of a parallel inverter system is shown in Fig. 1. This system consists of two parallel inverter modules, which share a common dc bus, and the ac sides of the modules are connected to the common ac output lines through individual filter inductors.

A. Current Path in Parallel Inverters

As an example, phase A has four circulating current paths in the system. These current paths can be divided into two groups based on the inclusions of the voltage source, as shown in Fig. 2. Phases B and C can be analyzed similarly.

The first group current paths, i.e., Path 1 and Path 2, do not have any voltage sources in them, as shown in Fig. 2(a).

Path 1: P-A_1-A-A_2-P.

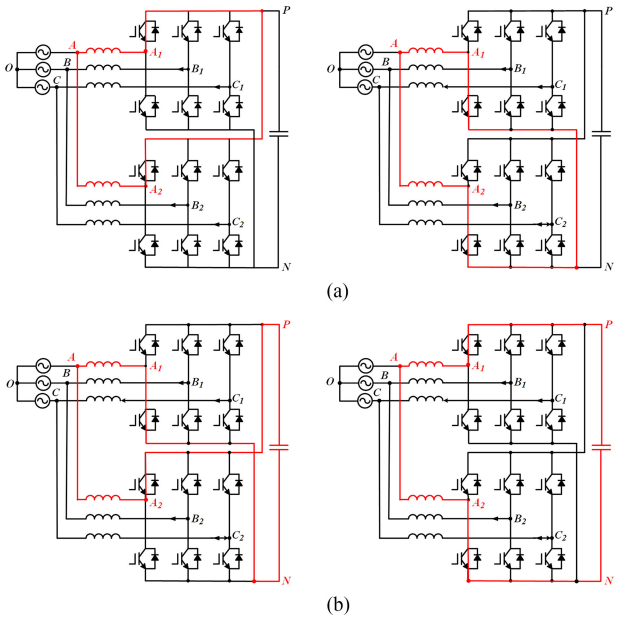

Fig. 2. Circulating current paths in parallel inverters. (a) Circulating current paths without DC source. (b) Circulating current paths containing DC source

Path 2: N-A_1-A-A_2-N.

In Path 1 and Path 2, given that no voltage sources are included, the circulating current will not change.

The second group current paths, including Path 3 and Path 4, have dc voltage sources in them, as shown in Fig. 2(b).

Path 3: P-A_1-A-A_2-N-P.

Path 4: P-A_2-A-A_1-N-P.

In this group, the current will flow through the corresponding phases of the two inverter modules (e.g., phase A of inverter 1 and inverter 2). This type of circulating current is called the interphase circulating current, and is the dominant circulating current in parallel inverters.

B. Definition of Circulating Current

Herein, only the interphase ZSCC are of interest. The interphase circulating current refers to the current flows between the same phase (e.g., phase A) of the two parallel inverter modules, which can be defined as

$$i_{cx} = \frac{i_{x1} - i_{x2}}{2},\ x = a, b, c \tag{1}$$

where i_{x1} and i_{x2} are the phase x current of inverter modules 1 and 2, respectively.

The flowing path of the interphase circulating current are Path 3 and Path 4 as mentioned above. The dc voltage source and filter inductors are included in the path, therefore the interphase circulating current can be calculated by the following equation:

$$V_{x1} - V_{x2} = (L_{x1} + L_{x2})\frac{di_{cx}}{dt} \tag{2}$$

where V_{x1} and V_{x2} refer to the phase x output voltages of the two inverter modules, respectively.

The ZSCC is the sum of three phase currents, which can be defined as

$$i_0 = i_{a1} + i_{b1} + i_{c1} = -(i_{a2} + i_{b2} + i_{c2}) \tag{3}$$

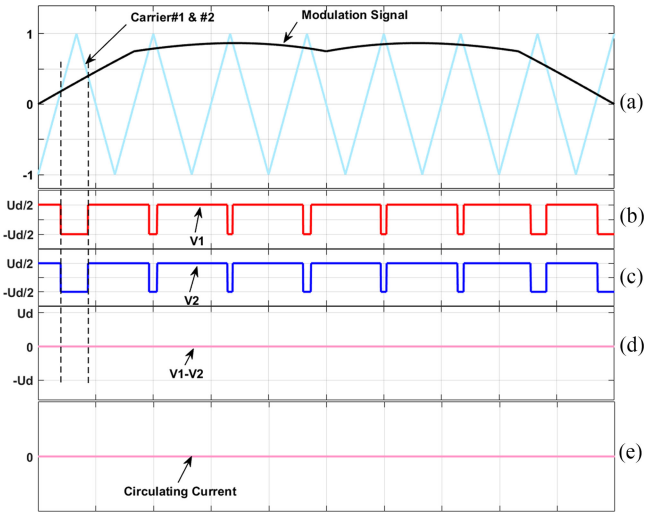

Fig. 3. Generation process of circulating current (θ = 0).

where i_{a1}, i_{b1}, and i_{c1} are the currents of phases A, B, and C, respectively, in the inverter module 1; i_{a2}, i_{b2}, and i_{c2} are the currents of phases A, B, and C, respectively, in the inverter module 2.

Therefore, the ZSCC can be rewritten by the interphase currents as follows:

$$\begin{aligned} i_0 &= \frac{1}{2}((i_{a1} - i_{a2}) + (i_{b1} - i_{b2}) + (i_{c1} - i_{c2})) \\ &= \frac{1}{2}(i_{ca} + i_{cb} + i_{cc}). \end{aligned} \tag{4}$$

C. Generation Process of High-Frequency Circulating Current

During a PWM process, either SPWM or SVM, the modulation wave and the carrier wave are the most critical signals. In a typical PWM process, the modulation signal value is compared with the carrier signal value. Subsequently, the output voltage pulse, either a high- or low-level pulse used to drive the switching devices, is generated according to the comparison result.

In a parallel-operated inverter system, if the parallel inverter modules have different modulation waveforms, a low-frequency (frequency of the modulation wave, which is typically 50 or 60 Hz) circulating current occurs. However, if the parallel inverter modules have different carrier waveforms, a high-frequency (frequency of the carrier wave, which is typically several Kilohertz) circulating current will instead be generated. This study will focus on the high-frequency circulating current caused by carrier phase difference; therefore, the modulation waves of the parallel inverter modules are assumed to be identical.

The detailed generation process of the circulating current is depicted in Figs. 3 and 4, including the 1) modulation signal of SVM and the carrier waveforms with phase difference θ, 2) output voltage pulse of inverter module #1, 3) output voltage pulse of inverter module #2, 4) output voltage pulse deviations of modules #1 and #2, and 5) resultant circulating current.

In Fig. 3, the carrier phase difference between two parallel inverter modules is zero. As the modulation signals of modules #1 and #2 are assumed to be identical as mentioned in Section II,

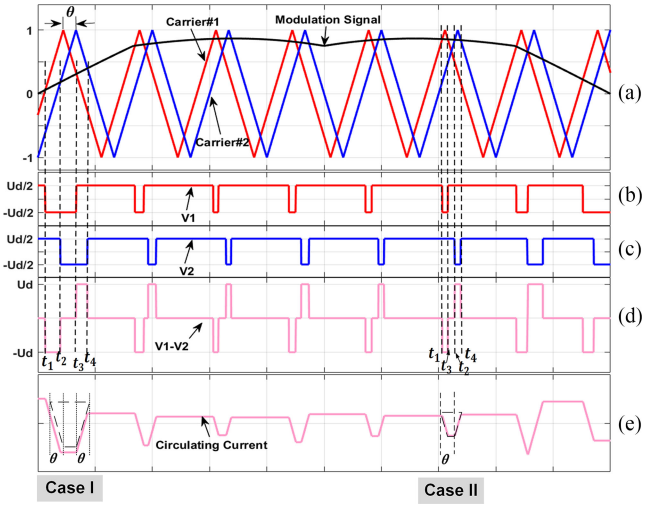

Fig. 4. Generation process of circulating current ($\theta \neq 0$).

the output voltage pulses V_1 and V_2 will be synchronous to each other, as shown in Fig. 3(b) and (c), hence the output voltage deviation V_1 - V_2 is zero. Therefore, the circulating current is zero according to (2).

In Fig. 4, the carrier phase difference between two parallel inverter modules is not zero. Although the modulation signals of modules #1 and #2 are still identical, the time instants when the modulation waveform intersects with carriers #1 and #2 are different, as shown in Fig. 4(a). The output voltage pulses V_1 and V_2 will no longer be synchronous to each other, as shown in Fig. 4(b) and (c), therefore the output voltage deviation V_1 - V_2 shown in Fig. 4(d) is not zero, and will cause the circulating current to flow through the parallel inverter modules, as shown in Fig. 4(e). The notations t_1 and t_2 refer to the time instant when the modulation signal intersects with the ascending line of triangular carriers #1 and #2, respectively, while t_3 and t_4 refer to the time instant when the modulation signal intersects with the descending line of triangular carriers #1 and #2, respectively.

As shown in Fig. 4(a), the two carriers with phase difference have two intersection points, one of which is positive and the other is negative. Depending on whether the modulation signal is between or beyond the two intersection points, the complete modulating process can be separated into two: Case I and Case II. In Case I, the modulation signal lies between the two intersection points of the two carriers. In Case II, the modulation signal is beyond the two intersection points, as shown in Fig. 4. These two cases must be differentiated because the time sequences of t_1, t_2, t_3, and t_4 are different in both cases, and this will influence the mathematical derivation in the next section.

The sketch diagram of modulation processes with different carrier phase differences is shown in Fig. 5. In general, as shown in Fig. 5, two observations can be summarized, which will be used in the following sections.

Observation 1: The modulation process is composed of both Case I and Case II. They transition to each other at certain times.

Observation 2: During the modulation process, the time durations of Case I and Case II are relevant to the phase difference θ between two carriers. If θ is smaller than $\frac{\pi}{2}$, then Case I lasts longer than Case II. If θ is larger than $\frac{\pi}{2}$, then Case II lasts longer

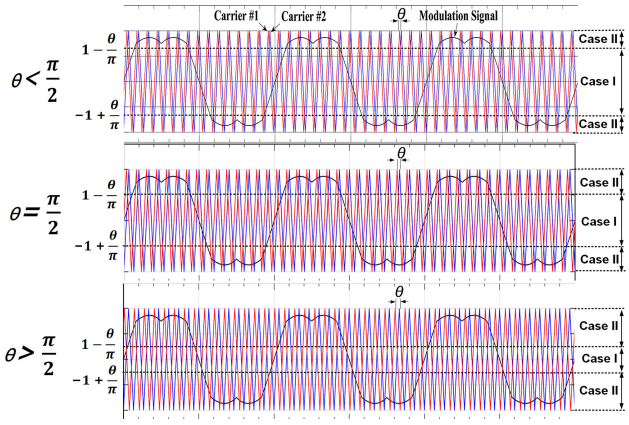

Fig. 5. Sketch diagram of modulation processes with different phase differences.

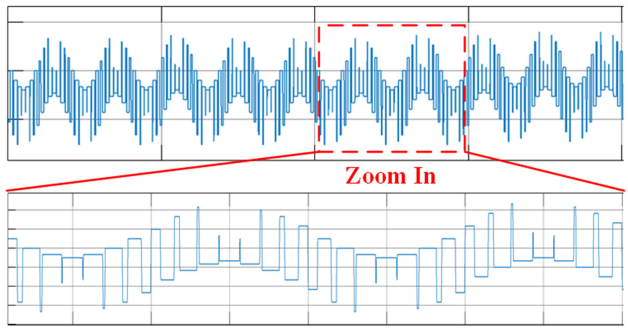

Fig. 6. Sketch diagram of high-frequency circulating current.

than Case I. The time durations of Case I and Case II will be equal when θ is $\frac{\pi}{2}$.

III. Modeling of Circulating Current Caused by Carrier Phase Difference

The circulating current caused by carrier phase difference is a series of high-frequency trapeziform waveform accompanied by low-frequency envelopes [25], [26]. The sketch diagram of such circulating current is shown in Fig. 6. On the one hand, voltage pulses will generate trapeziform currents, as shown in Fig. 4(e) and the bottom zoomed-in picture in Fig. 6. On the other hand, the magnitude of the circulating current changes with the modulation signal accordingly. Therefore, the circulating current is a series of trapeziform components slowly fluctuating with respect to the modulation signal. As it is difficult to simultaneously handle the slowly fluctuating trend and the instantaneous pulsating current, they will be treated in Sections III-A and III-B, separately.

The mathematical model of the circulating current for Case I will be derived in detail in this section, and the derivation for Case II will be presented in the appendix because of space constraints.

A. Mathematical Model of Circulating Current (Slow Fluctuating Trend)

It is noteworthy that although the modulation wave of the SVM is not explicit, it has been proven that a zero-sequence

signal-injected sinusoidal wave can be used as the equivalent modulation wave.

To simplify, the initial phase of the sinusoidal modulation signal of phase A is set to 0. For example, in phase A, the expression for sinusoidal modulation signal is

$$u_a^* = M\sin(\omega_s t) \tag{5}$$

where M is the modulation index and ω_s is the angular frequency of the grid voltage.

The zero-sequence component e_i injected into the sinusoidal modulation signal can be expressed as

$$e_i = -\frac{1}{2}[\max(u_a^*, u_b^*, u_c^*) + \min(u_a^*, u_b^*, u_c^*)]. \tag{6}$$

The added zero-sequence component is a triangular wave, its frequency is three times that of the fundamental wave, and its amplitude is a quarter of that of the sinusoidal modulation signal. Therefore, the expression for the zero-sequence component can be given as

$$\text{when } t \in \left[\frac{2k_1\pi}{3\omega_s} - \frac{\pi}{6\omega_s}, \frac{2k_1\pi}{3\omega_s} + \frac{\pi}{6\omega_s}\right]$$
$$e_i = \frac{3M\omega_s}{2\pi}\left(t - \frac{2k_1\pi}{3\omega_s}\right) \tag{7}$$
$$\text{when } t \in \left[\frac{2k_1\pi}{3\omega_s} + \frac{\pi}{6\omega_s}, \frac{2k_1\pi}{3\omega_s} + \frac{\pi}{2\omega_s}\right]$$
$$e_i = -\frac{3M\omega_s}{2\pi}\left(t - \frac{\pi}{3\omega_s} - \frac{2k_1\pi}{3\omega_s}\right) \tag{8}$$

where $k_1 \in Z$.

Hence, the final modulation signal with added zero-sequence signal can be expressed as $u_a = u_a^* + e_i$, which is a saddle-shaped waveform as shown in Fig. 5.

According to the definitions of t_1, t_2, t_3, and t_4, the modulation wave intersects with the carrier waves at these four time instants. Therefore, t_1, t_2, t_3, and t_4 shown in Fig. 4(d) satisfy the following equations:

$$\begin{cases} M\sin(\omega_s t_1) + \frac{3M\omega_s}{2\pi}\left(t_1 - \frac{2k_1\pi}{3\omega_s}\right) = \left(1 + \frac{\theta}{\pi} - 4k_2\right) + \frac{2\omega_c}{\pi}t_1 \\ M\sin(\omega_s t_2) + \frac{3M\omega_s}{2\pi}\left(t_2 - \frac{2k_1\pi}{3\omega_s}\right) = \left(1 - \frac{\theta}{\pi} - 4k_2\right) + \frac{2\omega_c}{\pi}t_2 \\ M\sin(\omega_s t_3) + \frac{3M\omega_s}{2\pi}\left(t_3 - \frac{2k_1\pi}{3\omega_s}\right) = \left(1 - \frac{\theta}{\pi} + 4k_2\right) - \frac{2\omega_c}{\pi}t_3 \\ M\sin(\omega_s t_4) + \frac{3M\omega_s}{2\pi}\left(t_4 - \frac{2k_1\pi}{3\omega_s}\right) = \left(1 + \frac{\theta}{\pi} + 4k_2\right) - \frac{2\omega_c}{\pi}t_4 \end{cases} \tag{9}$$

where $\theta \in [0, \pi]$, $k_2 \in Z$, and ω_c is the angular frequency of the triangular carriers. The exact positions of t_1, t_2, t_3, and t_4 are shown in Fig. 4(d).

By substracting the first formula from the second one in (9), the following can be deduced:

$$M(\sin(\omega_s t_2) - \sin(\omega_s t_1)) + \frac{3M\omega_s}{2\pi}(t_2 - t_1) = -\frac{2\theta}{\pi} + \frac{2\omega_c}{\pi}(t_2 - t_1) \tag{10}$$

which can be simplified to

$$2M\sin\left(\omega_s\frac{t_2 - t_1}{2}\right)\cos\left(\omega_s\frac{t_2 + t_1}{2}\right) + \frac{3M\omega_s}{2\pi}(t_2 - t_1) = -\frac{2\theta}{\pi} + \frac{2\omega_c}{\pi}(t_2 - t_1). \tag{11}$$

Since $t_2 - t_1$ is very small, $\sin(\omega_s\frac{t_2-t_1}{2}) \approx \omega_s\frac{t_2-t_1}{2}$, then

$$t_2 - t_1 = \frac{4\theta}{4\omega_c - 2\pi M\omega_s\cos\left(\omega_s\frac{t_2+t_1}{2}\right) - 3M\omega_s}. \tag{12}$$

Repeating the same process yields

$$t_4 - t_3 = \frac{4\theta}{4\omega_c + 2\pi M\omega_s\cos\left(\omega_s\frac{t_4+t_3}{2}\right) + 3M\omega_s}. \tag{13}$$

Therefore, the change in the circulating current in one switching period can be expressed as

$$\Delta i_c = i(t_4) - i(t_1) = \frac{V_1 - V_2}{L_1 + L_2}\left[(t_4 - t_3) - (t_2 - t_1)\right]. \tag{14}$$

In hindsight, from Case I shown in Fig. 4(d), it is clear that $t_4 - t_3$ is the duration of the positive voltage pulse in one switching period, and $t_2 - t_1$ is the duration of the negative voltage pulse. In (14), $(t_4 - t_3) - (t_2 - t_1)$ corresponds to the time duration of the effective positive voltage pulse, therefore Δi_c calculated by (14) can only reflect the average changing trend in one switching period, while the dynamic changing process from t_1 to t_2 and from t_3 to t_4 are neglected. The dynamic changing process will be considered in Sections III-B.

By substituting (12) and (13) into (14), we obtain (15) shown at the bottom of this page.

Since $2\pi M\omega_s\cos\left(\frac{t_4+t_3}{2}\omega_s\right) + 3M\omega_s \ll 4\omega_c$ and $2\pi M\omega_s\cos(\frac{t_2+t_1}{2}\omega_s) + 3M\omega_s \ll 4\omega_c$,

$$\therefore \Delta i_c \approx -\frac{\theta U_d[\pi M\omega_s\left(\cos\frac{t_1+t_2}{2}\omega_s + \cos\frac{t_3+t_4}{2}\omega_s\right) + 3M\omega_s]}{2(L_1 + L_2)\omega_c^2}. \tag{16}$$

Because t_1, t_2, t_3, and t_4 are very close to each other, $\cos\frac{t_1+t_2}{2}\omega_s + \cos\frac{t_3+t_4}{2}\omega_s \approx 2\cos(\omega_s t)$, where t is any time instant during the switching period.

Therefore, (16) can be simplified to

$$\therefore \Delta i_c \approx -\frac{\theta U_d[2\pi M\omega_s\cos(\omega_s t) + 3M\omega_s]}{2(L_1 + L_2)\omega_c^2}. \tag{17}$$

$$\therefore \Delta i_c = -\frac{4\theta U_d[2\pi M\omega_s\left(\cos\frac{t_1+t_2}{2}\omega_s + \cos\frac{t_3+t_4}{2}\omega_s\right) + 6M\omega_s]}{(L_1 + L_2)[4\omega_c + 2\pi M\omega_s\cos\left(\frac{t_4+t_3}{2}\omega_s\right) + 3M\omega_s][4\omega_c - 2\pi M\omega_s\cos\left(\frac{t_2+t_1}{2}\omega_s\right) - 3M\omega_s]} \tag{15}$$

The rate of change of the circulating current is

$$\frac{di_c}{dt} = \frac{\Delta i_c}{2\pi/\omega_c} = -\frac{\theta U_d[2\pi M\omega_s \cos(\omega_s t) + 3M\omega_s]}{4\pi(L_1+L_2)\omega_c}. \quad (18)$$

Therefore, the circulating current can be expressed by

$$i_c = \int \frac{di_c}{dt}dt = -\frac{M\theta U_d}{2(L_1+L_2)\omega_c}\sin(\omega_s t) - \frac{3U_d\theta M\omega_s}{4\pi(L_1+L_2)\omega_c}(t - \frac{2k_1\pi}{3\omega_s}) \quad (19)$$

when $t \in [\frac{2k_1\pi}{3\omega_s} - \frac{\pi}{6\omega_s}, \frac{2k_1\pi}{3\omega_s} + \frac{\pi}{6\omega_s}]$, and

$$i_c = -\frac{M\theta U_d}{2(L_1+L_2)\omega_c}\sin(\omega_s t) - \frac{3U_d\theta M\omega_s}{4\pi(L_1+L_2)\omega_c} \times \left(t - \frac{\pi}{3\omega_s} - \frac{2k_1\pi}{3\omega_s}\right) \quad (20)$$

when $t \in [\frac{2k_1\pi}{3\omega_s} + \frac{\pi}{6\omega_s}, \frac{2k_1\pi}{3\omega_s} + \frac{\pi}{2\omega_s}]$

From (19) and (20), the circulating current calculated can be rewritten as $i_c = i_{c1} + i_{c2}$.

The first part is the fundamental sinusoidal circulating current

$$i_{c1} = -\frac{M\theta U_d}{2(L_1+L_2)\omega_c}\sin(\omega_s t). \quad (21)$$

The second part is a triangle circulating current, and its frequency is three times that of the fundamental wave

$$i_{c2} = -\frac{3U_d\theta M\omega_s}{4\pi(L_1+L_2)\omega_c}\left(t - \frac{2k_1\pi}{3\omega_s}\right) \quad (22)$$

when $t \in [\frac{2k_1\pi}{3\omega_s} - \frac{\pi}{6\omega_s}, \frac{2k_1\pi}{3\omega_s} + \frac{\pi}{6\omega_s}]$, and

$$i_{c2} = \frac{3U_d\theta M\omega_s}{4\pi(L_1+L_2)\omega_c}\left(t - \frac{\pi}{3\omega_s} - \frac{2k_1\pi}{3\omega_s}\right) \quad (23)$$

when $t \in [\frac{2k_1\pi}{3\omega_s} + \frac{\pi}{6\omega_s}, \frac{2k_1\pi}{3\omega_s} + \frac{\pi}{2\omega_s}]$.

B. Mathematical Model of Circulating Current (Instantaneous Pulsating Current)

The sketch diagram of the high-frequency pulsating currents for both Case I and Case II is shown in Fig. 7. As mentioned above, the criterion for differentiating Case I and Case II is whether the modulation wave is between or beyond the positive and negative intersection points of the two carrier triangular waves. Fig. 7 only illustrates the positive intersection point, and the negative one can be analyzed similarly. It is noteworthy that Fig. 7(a) will be used here and Fig. 7(b) will not be used before the Appendix; however, it is presented here for comparison.

From the top diagram of Fig. 7(a) and according to the theorem of similar triangles

$$\frac{1-H}{H} = \frac{\theta}{\pi-\theta} \quad \text{and} \quad \frac{\theta}{T_1} = \frac{\frac{\theta}{\pi}}{1-\frac{\theta}{\pi}-u_a}.$$

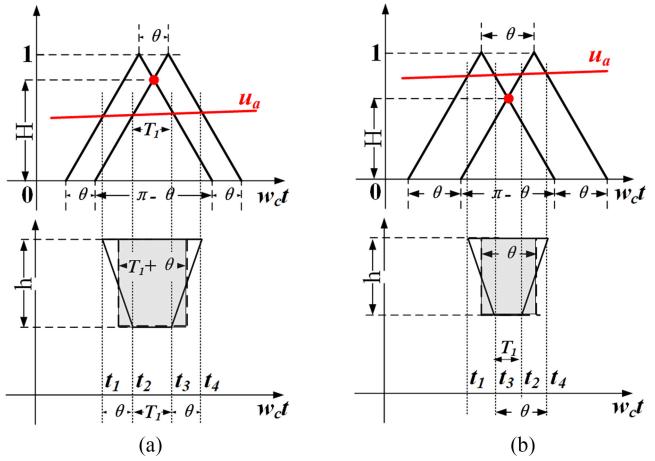

Fig. 7. Sketch diagram of pulsating current. (a) Case I. (b) Case II.

H and T_1 can be resolved from the previous equations, which are

$$H = 1 - \frac{\theta}{\pi} \quad (24)$$

$$T_1 = \pi(1-u_a) - \theta. \quad (25)$$

Fig. 4(d) and (e) shows that the negative voltage pulse causes the circulating current to decrease and the positive voltage pulse causes it to increase, resulting in high-frequency trapeziform currents. Although Section III-A has considered the circulating current variation from t_1 to t_4, it neglects the instantaneous change during t_1 to t_2 and t_3 to t_4, which will be discussed here.

Both the effective time of the positive and negative voltage pulses are $\frac{\theta}{\omega_c}$, therefore the peak-to-peak value of the trapeziform current can be deduced by

$$h = \frac{U_d}{L_1+L_2} \cdot \Delta t = \frac{U_d\theta}{(L_1+L_2)\omega_c}. \quad (26)$$

For simplification, the trapeziform current can be approximated by a square wave, which is shown by the shaded area in the bottom picture of Fig. 7(a). As the carrier frequency is much larger than the modulation signal frequency, the modulation signal value is assumed to be constant in a carrier period. By applying the Fourier transform to the trapeziform current

$$i_{c3} = \frac{a_0}{2} + \sum_{n=1}^{\infty}(a_n \cos n\omega_c t + b_n \sin n\omega_c t) \quad (27)$$

where

$$\begin{cases} a_n = \frac{1}{\pi}\int_{-\pi}^{\pi} -h\cos(n\omega_c t)d(\omega_c t) \\ = \frac{1}{\pi}\int_{-\pi}^{\pi} \frac{-U_d\theta}{(L_1+L_2)\omega_c}\cos(n\omega_c t)d(\omega_c t) \qquad (n = 0, 1, 2, \ldots) \\ b_n = \frac{1}{\pi}\int_{-\pi}^{\pi} -h\sin(n\omega_c t)d(\omega_c t) \\ = \frac{1}{\pi}\int_{-\pi}^{\pi} \frac{-U_d\theta}{(L_1+L_2)\omega_c}\sin(n\omega_c t)d(\omega_c t) \qquad (n = 1, 2, \ldots). \end{cases} \quad (28)$$

Therefore

$$a_0 = \frac{1}{\pi}\int_{-\pi}^{\pi}\frac{-U_d\theta}{(L_1+L_2)\omega_c}d(\omega_c t) = \frac{-U_d\theta}{\pi(L_1+L_2)\omega_c}\cdot(T_1+\theta)$$
$$= -\frac{U_d\theta}{2\omega_c(L_1+L_2)} + \frac{U_d\theta M}{2\omega_c(L_1+L_2)}(\sin\omega_s t + \frac{3\omega_s t}{2\pi}) \tag{29}$$

$$a_n = \frac{1}{\pi}\int_{-\pi}^{\pi}\frac{-U_d\theta}{(L_1+L_2)\omega_c}\cos(n\omega_c t)d(\omega_c t)$$
$$= \frac{-U_d\theta}{\pi(L_1+L_2)\omega_c}\cdot\frac{1}{n}\cdot\sin(n\omega_c t)\Big|_{-\frac{T_1+\theta}{2}}^{\frac{T_1+\theta}{2}}$$
$$= -\frac{U_d\theta}{\omega_c(L_1+L_2)}\frac{2}{n\pi}\sin\left(\frac{n\pi}{2}\left(1-M\sin(\omega_s t)-\frac{3M\omega_s t}{2\pi}\right)\right)$$
$$\times\ (n=1,2,\ldots). \tag{30}$$

That is

$$\begin{cases} a_0 = -\frac{U_d\theta}{2\omega_c(L_1+L_2)} + \frac{U_d\theta M}{2\omega_c(L_1+L_2)}(\sin\omega_s t + \frac{3\omega_s t}{2\pi}) \\ a_n = -\frac{U_d\theta}{\omega_c(L_1+L_2)}\frac{2}{n\pi}\sin\left(\frac{n\pi}{2}\left(1-M\sin(\omega_s t)-\frac{3M\omega_s t}{2\pi}\right)\right) \\ b_n = 0, (n=1,2,\ldots). \end{cases} \tag{31}$$

C. Component Analysis of Circulating Current

From (21)–(23) and (31), the characteristics of the circulating current for Case I can be summarized as follows.

1) The spectrum components of the circulating current consist of the fundamental frequency, triple harmonic frequency, carrier frequency, and odd multiples of carrier frequency.
2) The amplitude of the circulating current is in direct proportion to the carrier phase difference θ and dc voltage U_d, and is in inverse proportion to the impedance of the circulating current path L_1+L_2 and the angular frequency of carrier ω_c.

For Case II, the deduction process is similar to Case I, and the step-by-step derivation will be presented in the Appendix at the end of this paper. The characteristics of the circulating current for Case II can be expressed as follows, where the last sentence highlights its differences from Case I.

1) The spectrum components of the circulating current consist of the carrier frequency and odd multiples of the carrier frequency. The triple harmonic frequency circulating current is negligible.
2) The amplitude of the circulating current is in direct proportion to the dc voltage U_d, and is in inverse proportion to the impedance of the circulating current path L_1+L_2 and the angular frequency of carrier ω_c. The amplitude of the carrier-frequency circulating current is in direct proportion to $\sin\frac{\theta}{2}$.

According to ***Observation 1*** and ***Observation 2*** mentioned above in Section II, during a complete modulation period, Case I and II coexist, and Case I transitions to Case II at a certain point. On the one hand, according to the spectrum analysis mentioned above, the third-order harmonic circulating current will decrease significantly at the point when Case I transitions to Case II. On the other hand, the duration of Case I and II are equal when θ is 90°, therefore Case I will be more predominant when θ is smaller than 90°, and Case II will be more predominant when θ is larger than 90°. Referring to Fig. 5 may be helpful in understanding this intuitively.

Subsequently, the characteristics of the third-order circulating current can be concluded as follows.

Conclusion 1: With the carrier phase difference θ increasing from 0 to 180°, the amplitude of the third-order circulating current will first increase from 0 to a maximum value (when θ equals to 90°) and then decrease to 0 again.

In Case I, the amplitude of the carrier-frequency circulating current is in direct proportion to θ, and is in direct proportion to $\sin\frac{\theta}{2}$ for Case II. Further, considering the transition from Case I to Case II analyzed above, the characteristics of the carrier frequency circulating current can be concluded as follows.

Conclusion 2: With the carrier phase difference θ increasing from 0 to 180°, the amplitude of the carrier-frequency circulating current will increase until the maximum but with a decreasing rate of change (slope).

Based on the aforementioned mathematical derivation, the characteristics of the circulating current caused by carrier phase difference are summarized as ***Conclusion 1*** and ***Conclusion 2***, which reveal the specific relationship between the circulating current and carrier phase difference, the spectrum components

TABLE I
SIMULATION AND EXPERIMENTAL PARAMETERS

Parameters	Symbol	Value
AC line-to-line voltage	V_{pp}	190V
DC bus voltage	U_d	400V
Filter inductance-Module 1	L_1	6mH
Filter inductance-Module 2	L_2	6mH
Fundamental frequency	f_s	50Hz
Carrier frequency	f_c	5kHz
Sampling frequency	f_{sample}	20kHz
Control period	T_c	50μs
Simulation step	T_s	2μs

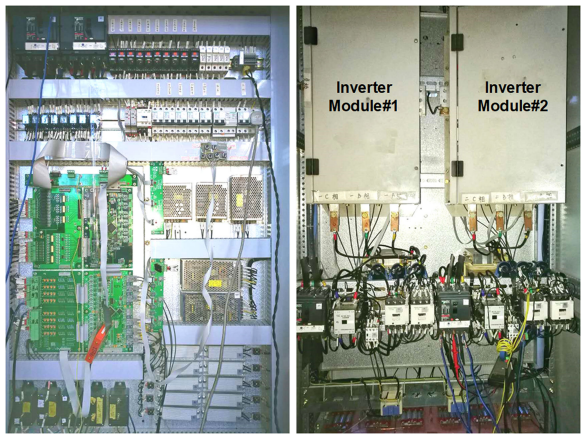

Fig. 8. Pictures of experimental hardware platform.

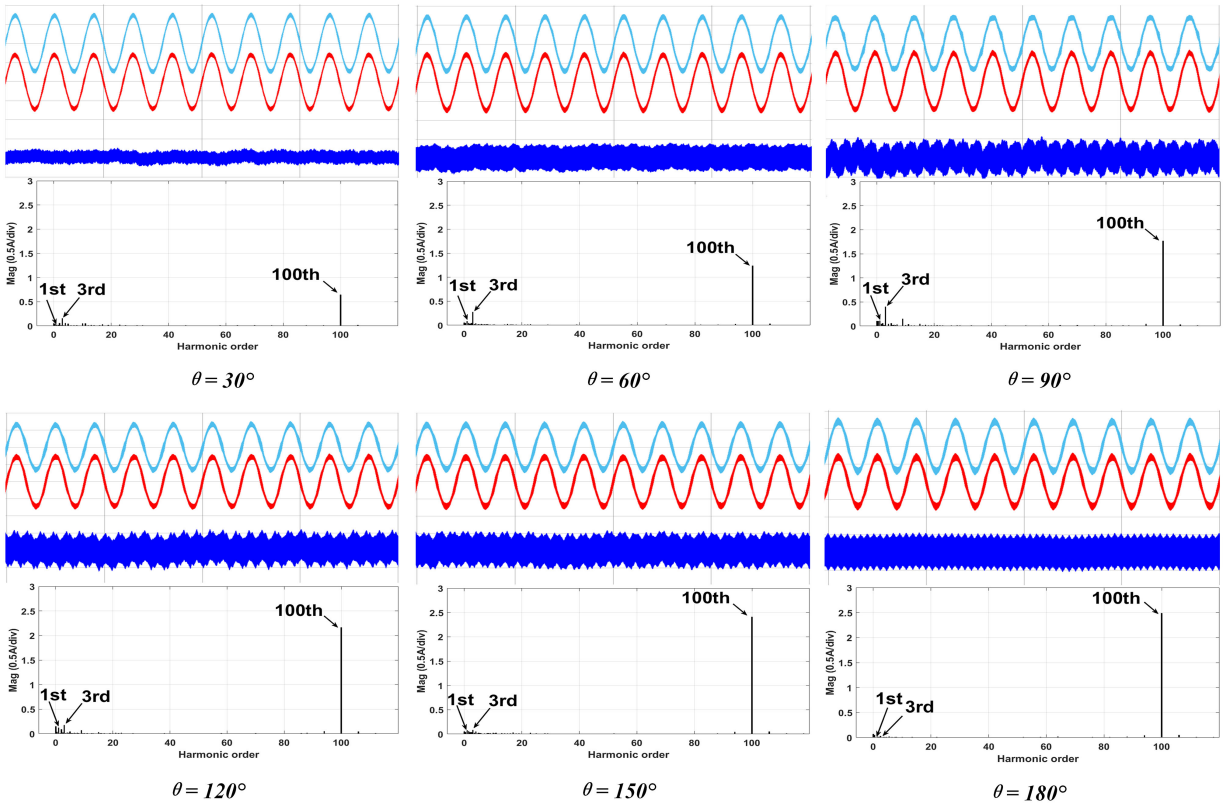

Fig. 9. Phase A currents of modules 1 and 2, circulating current, and FFT Spectrum. (I_{a1}, I_{a2}: 5 A/ div | I_0 : 2.5 A/ div | FFT:0.5 A/ div).

of the high-frequency circulating current, and how the circulating current changes with respect to different carrier phase differences.

IV. Simulation and Experimental Results

To verify the aforementioned mathematical model and theoretical analysis and to demonstrate the closed-loop adjustment of carrier phase difference for suppressing the high-frequency circulating current, simulations and experiments are conducted, and the simulation and experimental parameters are shown in Table I.

A laboratory prototype with two parallel-connected 10-kW inverter modules is constructed for the experiment, in which the digital signal processor TMS320LF2812 from Texas Instruments Incorporated is used as the control kernel. Fig. 8 shows the pictures of the hardware of the prototype.

In the simulation and experimental results, the third-order and one-hundredth-order harmonics of the circulating current will be analyzed. The fundamental frequency is 50 Hz and the carrier frequency is 5 kHz; therefore, the one-hundredth-order harmonic refers to the switching frequency.

A. Model Verification

The circulating current waveforms and their fast Fourier transform (FFT) spectrums when the carrier phase difference θ is 30°, 60°, 90°, 120°, 150°, and 180° are shown in Fig. 9. The individual FFT spectrum shows that the amplitude of the third-order circulating current is approximately 1 A when the phase difference θ is 90° and then decreases when θ increases. When θ is 180°, a third-order component does not exist, and the circulating current primarily consists of the carrier frequency component. The changing trend of these components in the simulation results further verifies the modeling and analysis results (especially ***Conclusion 1*** and ***Conclusion 2***).

TABLE II
Simulation and Experimental Results of Circulating Current Components With Different Carrier Phase Differences (S denotes simulation and E denotes experiment)

Harmonic (A)		Carrier Phase Difference						
		0°	30°	60°	90°	120°	150°	180°
1ST	S	0	0.07	0.05	0.04	0.07	0.07	0.01
	E	0.10	0.095	0.09	0.085	0.075	0.08	0.09
3RD	S	0	0.16	0.37	0.46	0.28	0.11	0.01
	E	0.067	0.28	0.38	0.473	0.413	0.26	0.01
100TH	S	0	0.63	1.23	1.76	2.16	2.41	2.49
	E	0.007	0.653	1.127	1.76	2.133	2.287	2.46

The amplitudes of the third- and one-hundredth-order circulating currents with respect to different phase differences θ, which increase from 0° to 180° at increments of 30°, are shown in Table II. Their trends are depicted in Fig. 10, including the simulation and experimental results. As shown, the amplitude of the third-order circulating current first increases from 0 (when θ is 0°) to a maximum value (when θ is 90°), and then

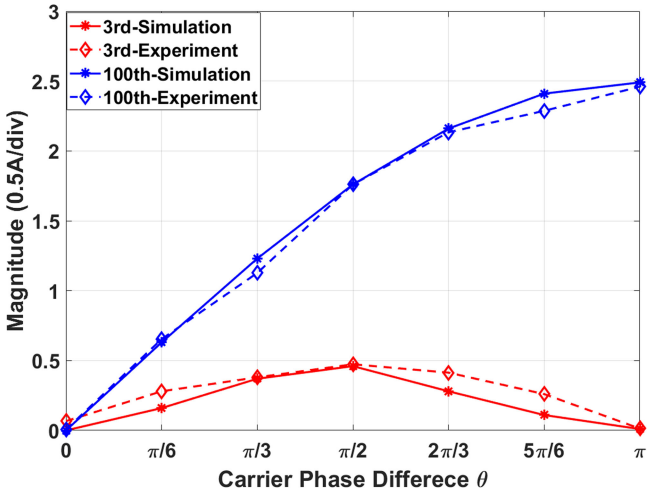

Fig. 10. Trends of circulating current components versus carrier phase differences (simulation and experimental results).

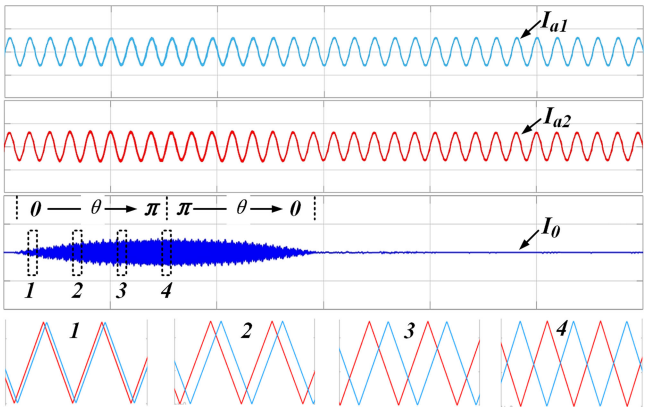

Fig. 11. Simulation results of circulating current when θ changes periodically. (I_{a1}, I_{a2}: 5 A/ div, I_0: 2.5 A/ div, Time: 100 ms/ div).

decreases to 0 (when θ is 180°) again, which is consistent with ***Conclusion 1*** described in Section III. Further, the amplitude of the carrier-frequency circulating current increases to the maximum but with a decreasing slope, which verifies ***Conclusion 2*** mentioned above.

Figs. 11 and 12 show the simulation and experimental results of the circulating current, respectively, during a continuous angle-shifting process, in which the carrier phase difference first increases from 0° to 180°, and then decreases to 0° again. The current references of the two parallel modules are both 5 A (RMS value). The results show that the circulating current increases to a maximum value (when carrier phase difference is 180°), and then decreases with the decreasing carrier phase difference; further, the changing trend verifies the direct relationship between the circulating current and the carrier phase difference.

B. Closed-Loop Carrier Phase Adjustment

In practical conditions, closed-loop control must be adopted to regulate the carrier phase difference in real time. The system control diagram with a closed-loop control strategy is shown in

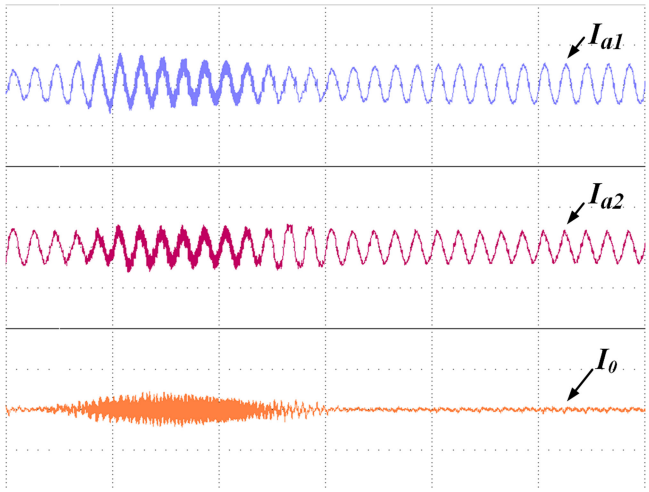

Fig. 12. Experimental results of circulating current when θ changes periodically. (I_{a1}, I_{a2}: 5 A/ div, I_0: 2.5 A/ div, Time: 100 ms/ div).

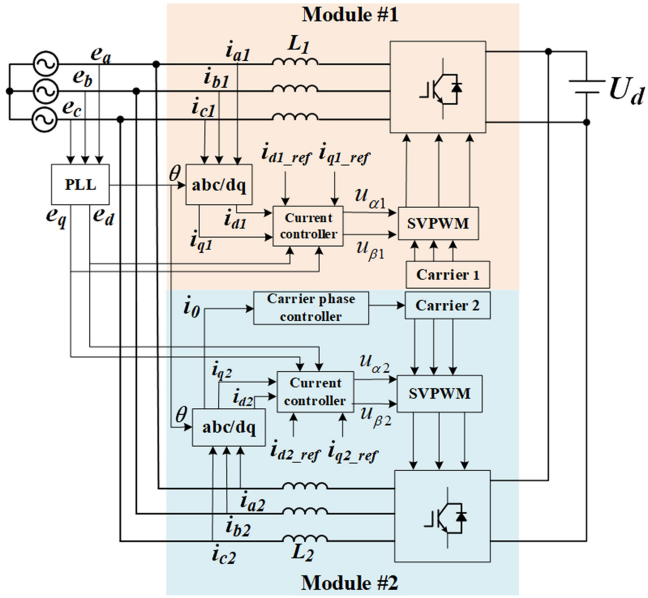

Fig. 13. System control diagram with a closed-loop carrier phase controller.

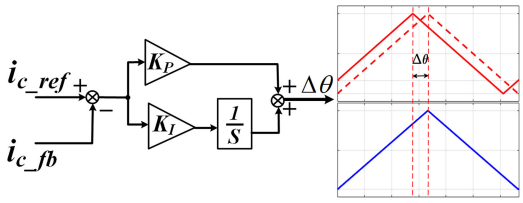

Fig. 14. Control diagram of a carrier phase controller.

Fig. 13. A simple PI controller is chosen as the carrier phase controller herein, and the control diagram of the carrier phase controller is shown in Fig. 14. Two points need to be emphasized: First, the absolute value of the measured circulating current is used as the feedback signal of the controller, because only the absolute value (not the instant value or average value) can reflect the changing trend of the circulating current magnitude. Second, the controller parameters (such as the proportional

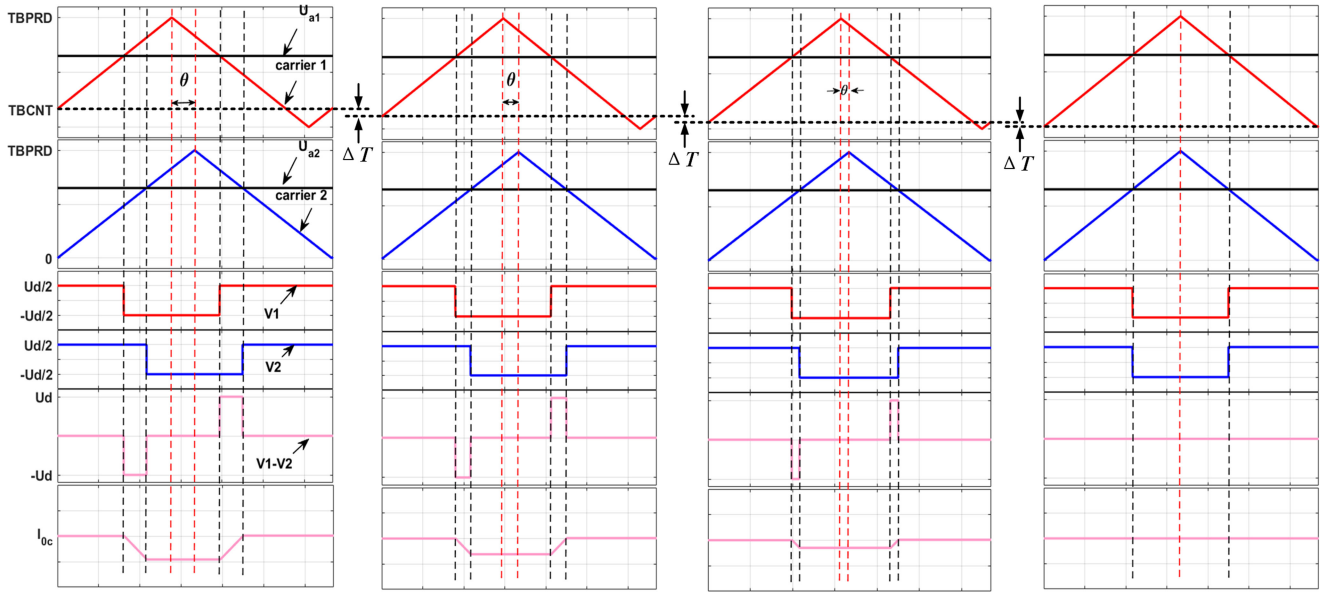

Fig. 15. Adjustment process of carrier phase difference.

gain) are highly dependent on practical applications; therefore, they must be selected and adjusted appropriately according to the system variables including the reference currents and control period. $\triangle\ \theta$ is the output of the controller that is used to adjust the carrier phase.

DSP and FPGA are the most popular hardware devices used to control power converters. Typically, the up-down counter is adopted to implement the carrier waveform. The modulation signal value will be updated in each control period and saved in a compare register. Subsequently, the hardware will compare the register value with the current counting value, and the comparison result is used to generate high- or low-level voltage pulses that are used to drive the switching devices (e.g., IGBT). In the default configuration, the counter first counts from 0 to a maximum value (TBPRD, which is the period register of the corresponding PWM generation module) in the up-count direction, and then counts from TBPRD to 0 in the down-count direction: this is a complete counting period. Therefore, the carrier phase can be adjusted by simply changing the initial value of the counter.

The sketch diagram of the carrier phase adjustment process is shown in Fig. 15. From left to right, assuming that carrier 2 is kept unchanged and carrier 1 is adjusted, the carrier phase difference θ is decreased continuously simply by decreasing (or increasing in other situations) the initial value of TBCNT of carrier 1. The adjusted amount of TBCNT is illustrated as $\triangle\ T$, the value of which corresponds to the output of the carrier phase controller. The carrier phase controller output $\triangle\ \theta$ must be converted to $\triangle\ T$ accordingly considering the TBPRD value, which is determined by the switching frequency. After several adjustment periods, the phase difference will be eliminated gradually.

When the reference currents of the two parallel modules are both 5 A, the experimental results of the closed-loop control is shown in Fig. 16. The high-frequency component is superimposed on the phase currents before control, and the

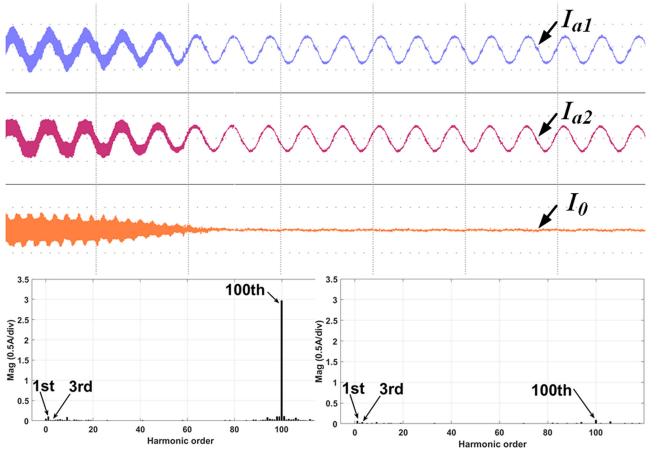

Fig. 16. Closed-loop control with identical reference currents. Waveforms: I_{a1}, I_{a2} (5 A/ div), I_0 (2.5 A/ div), Time (50 ms/ div) FFT: Before and after control, respectively (0.5 A/ div).

corresponding ZSCC is approximately 4 A. The peak value of circulating current can be suppressed to 0.6 A by the closed-loop control. The FFT shows that the dominant component of the circulating current is at the carrier frequency, and is effectively restrained to a negligible value.

When the reference currents of the two modules are not identical, in which the reference current of module 1 is set to 5 A, and the reference current of module 2 is set to 3 A, the results of the closed-loop control is shown in Fig. 17. As the reference currents of the two modules are dissimilar, a discrepancy exists between the modulation signals. Therefore, a low-frequency (three times that of the fundamental frequency) circulating current is generated in the system. Given that the carrier phase control has very limited effect on the low-frequency circulating current, the third-order component is only restrained from approximately 0.4 to 0.3 A. However, the switching frequency component is

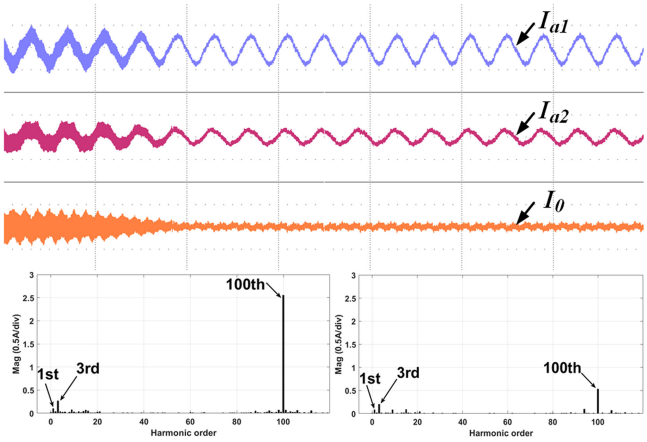

Fig. 17. Closed-loop control with different reference currents. Waveforms: I_{a1}, I_{a2} (5 A/ div), I_0 (2.5 A/ div), Time (50 ms/ div) FFT: Before and after control, respectively (0.5 A/ div).

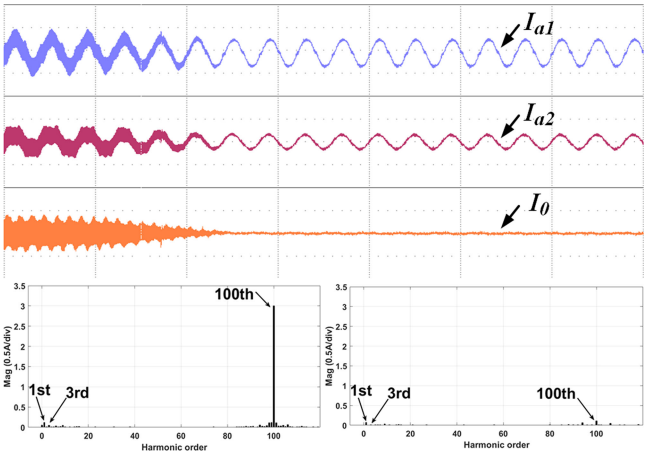

Fig. 18. Combined deadbeat and closed-loop control with different reference currents. Waveforms: I_{a1}, I_{a2} (5 A/ div), I_0 (2.5 A/ div), Time (50 ms/div) FFT: Before and after control, respectively (0.5 A/ div).

suppressed from approximately 2.5 to 0.5 A, which again proves that the carrier phase control can significantly reduce the high-frequency circulating current.

Deadbeat control is very effective in suppressing low-frequency circulating currents; therefore, combining deadbeat and closed-loop control can improve the circulating current suppression performance, especially when the third-order frequency and switching-frequency components of the circulating current both exist. As the deadbeat control is out of the scope of this paper, it will not be discussed in detail; only the experimental result is shown in Fig. 18. Compared to Fig. 17, both the third-order and the switching-frequency components are further reduced to a negligible value (approximately 0.2 A). The FFT spectrum shows that the deadbeat control effectively mitigates the third-order component at the beginning, and then the carrier phase control further reduces the high-frequency component.

From the simulation and experimental results above, we conclude that the components and characteristics of the circulating current are identical with theoretical analysis, and the closed-loop adjustment of the carrier phase difference is effective in suppressing the high-frequency circulating current, even when the current references of the parallel modules are not identical. However, other control strategies such as deadbeat control should be combined with the carrier phase control to achieve better overall performance for the suppression of both low- and high-frequency circulating currents.

V. Conclusion

Herein, the circulating current caused by the carrier phase difference in parallel converters is studied. A mathematical model is established, and the components and characteristics of the circulating current are also analyzed. The amplitude of the high-frequency circulating current is directly proportional to the carrier phase difference, and its frequency primarily consists of carrier frequency. A closed-loop carrier phase controller is proposed to suppress the high-frequency circulating current. The mathematical model and theoretical analysis are verified by simulations and experiments, and the effectiveness of the control method is also validated.

The interleaved operation of the parallel inverter modules is not discussed in this paper, because the carrier phases are intentionally shifted to each other for interleaving, which will inevitably cause significant circulating currents. However, the purpose of this study is to reduce the carrier phase difference as much as possible to suppress the circulating current, which contradicts with the purpose of interleaving. Nevertheless, interleaving carriers could be beneficial to the harmonic performance of grid currents. Therefore, the carrier phase control proposed herein may be combined with interleaving to obtain the optimized carrier phase difference and harmonic performance, to maintain the balance between a sufficiently small circulating current and the harmonic performance of the grid current, which will be considered in future works.

Furthermore, the parallel inverters system discussed herein only consists of two modules, and multimodule situations are not discussed. For an *N*-module system, the total circulating current flowing through any one module is the superimposition of the circulating currents between this module and all the other *N*–1 modules. Therefore, for the analysis of the circulating current between any two modules, the mathematical modeling and analysis proposed herein can be applied. However, the closed-loop carrier phase adjustment method herein is insufficient to control the total circulating current in an *N*-module system, because the interactions between all the modules are more complicated. Further research must be conducted to find a better approach to achieve carrier synchronization among multimodules.

Appendix

For the completeness of this paper and the convenience in understanding the mathematical deduction process, the derivation of Case II is affixed in this section. Similar to the derivation process of Case I, the content of this appendix is also divided into two parts that handle the slow fluctuating trend and the instantaneous pulsing part of the circulating current separately, similar to Section III-A and III-B.

A. Mathematical Model of Circulating Current (Slow Fluctuating Trend)

Equation (9) is rewritten here for convenience as follows:

$$\begin{cases} M\sin(\omega_s t_1)+\frac{3M\omega_s}{2\pi}\left(t_1-\frac{2k_1\pi}{3\omega_s}\right)=\left(1+\frac{\theta}{\pi}-4k_2\right)+\frac{2\omega_c}{\pi}t_1 \\ M\sin(\omega_s t_2)+\frac{3M\omega_s}{2\pi}\left(t_2-\frac{2k_1\pi}{3\omega_s}\right)=\left(1-\frac{\theta}{\pi}-4k_2\right)+\frac{2\omega_c}{\pi}t_2 \\ M\sin(\omega_s t_3)+\frac{3M\omega_s}{2\pi}\left(t_3-\frac{2k_1\pi}{3\omega_s}\right)=\left(1-\frac{\theta}{\pi}+4k_2\right)-\frac{2\omega_c}{\pi}t_3 \\ M\sin(\omega_s t_4)+\frac{3M\omega_s}{2\pi}\left(t_4-\frac{2k_1\pi}{3\omega_s}\right)=\left(1+\frac{\theta}{\pi}+4k_2\right)-\frac{2\omega_c}{\pi}t_4 \end{cases} \tag{A-1}$$

where $\theta\in[0,\pi]$, $k_2\in Z$, and ω_c is the angular frequency of triangular carrier. The exact positions of t_1, t_2, t_3 , and t_4 are shown in Fig. 4(d).

The sum of the first and third formulas in (A-1) can be expressed as

$$M\sin(\omega_s t_1)+\sin(\omega_s t_3))+\frac{3M\omega_s}{2\pi}(t_1+t_3) =\frac{2\omega_c}{\pi}(t_1-t_3)+2+2k_1M. \tag{A-2}$$

By substracting the third formula from the first one in (A-1), the following can be deduced:

$$M\sin(\omega_s t_1)-\sin(\omega_s t_3))+\frac{3M\omega_s}{2\pi}(t_1-t_3) =\frac{2\omega_c}{\pi}(t_1+t_3)+\frac{2\theta}{\pi}-8k_2. \tag{A-3}$$

Adding (A-2) and (A-3) yields

$$2M\sin(\omega_s t_1)+\frac{6M\omega_s}{\pi}t_1=\frac{4\omega_s}{\pi}t_1+\frac{2\theta}{\pi}-8k_2+2+2k_1M. \tag{A-4}$$

From (A-4), the expression for t_1 can be deduced as

$$t_1=\frac{\pi}{6M\omega_s-4\omega_c}\left(\frac{2\theta}{\pi}-8k_2+2+2k_1M-2M\sin(\omega_s t_1)\right). \tag{A-5}$$

By substracting (A-3) from (A-2), we obtain

$$2M\sin(\omega_s t_3)+\frac{3M\omega_s}{\pi}t_3=-\frac{4\omega_c}{\pi}t_3-\frac{2\theta}{\pi}+8k_2+2+2k_1M. \tag{A-6}$$

From (A-6), the expression for t_3 can be deduced as

$$t_3=\frac{\pi}{3M\omega_s+4\omega_c} \times\left(-\frac{2\theta}{\pi}+8k_2+2+2k_1M-2M\sin(\omega_s t_3)\right). \tag{A-7}$$

Repeating the similar process like (A-2) to (A-7), the expression for t_2 and t_4 can also be deduced as

$$t_2=\frac{\pi}{3M\omega_s-8\omega_c}\left(2-\frac{2\theta}{\pi}-8k_2+2k_1M-2M\sin(\omega_s t_2)\right) \tag{A-8}$$

$$t_4=\frac{\pi}{3M\omega_s+4\omega_c}\left(2+\frac{2\theta}{\pi}+8k_2+2k_1M-2M\sin(\omega_s t_4)\right) \tag{A-9}$$

The change of the circulating current in one switching period can be expressed by the deviation of the positive and negative voltage pulses, as shown in Fig. 4(d). For Case I, according to the time sequence of t_1, t_2, t_3, and t_4, the expression is

$$\Delta i_c=i(t_4)-i(t_1)=\frac{V_1-V_2}{L_1+L_2}\left[(t_4-t_3)-(t_2-t_1)\right]. \tag{A-10}$$

However, the time sequence of t_1, t_2, t_3, and t_4 for Case II is different from Case I, so the expression is different

$$\Delta i_c=i(t_4)-i(t_1)=\frac{V_1-V_2}{L_1+L_2}\left[(t_4-t_2)-(t_3-t_1)\right]. \tag{A-11}$$

After substituting (A-5), (A-7), (A-8), and (A-9) into (A-11), we get

$$\therefore\Delta i_c=\frac{U_d}{(L_1+L_2)}\left(-\frac{\pi-\theta}{4\omega_c}+\frac{M\pi(2\sin\omega_s t_1-\sin\omega_s t_2)}{4\omega_c} +\frac{2M\pi(2\sin\omega_s t_3-\sin\omega_s t_4)}{4\omega_c}\right). \tag{A-12}$$

Since $t_2-t_1=t_4-t_3=\theta/\omega_c$

$$2\sin\omega_s t_1-\sin\omega_s t_2=2\sin\omega_s t_1-\sin\omega_s\left(t_1+\frac{\theta}{\omega_c}\right) =2\sin\omega_s t_1-\sin\omega_s t_1\cos\frac{\omega_s\theta}{\omega_c}-\cos\omega_s t_1\sin\frac{\omega_s\theta}{\omega_c}. \tag{A-13}$$

Because $\omega_s\theta\ll\omega_c$, (A-13) can be simplified to $\sin\omega_s t_1$, therefore

$$\sin\omega_s t_3-\sin\omega_s t_4=2\cos\frac{\omega_s(t_3+t_4)}{2}\sin\frac{\omega_s(t_3-t_4)}{2}. \tag{A-14}$$

Because t_3 and t_4 are very close to each other, $\cos\frac{\omega_s(t_3+t_4)}{2}\approx\cos\omega_s t$, and $\sin\frac{\omega_s(t_3-t_4)}{2}\approx\frac{\omega_s(t_3-t_4)}{2}\approx-\frac{\omega_s\theta}{2\omega_c}$, where t is any time instant during the switching period.

Considering the approximation mentioned above, (A-12) can be further simplified to

$$\Delta i_c=\frac{U_d}{(L_1+L_2)}\frac{-M\pi\theta}{2\omega_c^2}\cos\omega_s t. \tag{A-15}$$

The rate of change of the circulating current is

$$\frac{di_c}{dt}=\frac{\Delta i_c}{2\pi/\omega_c}=\frac{-M\theta U_d\cos\omega_s t}{4(L_1+L_2)\omega_c}. \tag{A-16}$$

Therefore, the circulating current can be expressed by

$$i_c=\int\frac{di_c}{dt}dt=-\frac{M\theta U_d}{4(L_1+L_2)\omega_c}\sin\omega_s t. \tag{A-17}$$

Comparing (A-17) with (19) and (20) shows that the characteristics of the circulating current in Case II are different from Case I. In Case II, the spectrum components of the circulating current consist of carrier frequency and odd multiples of the carrier frequency, and there are no triple harmonic frequency circulating current.

B. Mathematical Model of Circulating Current (Instantaneous Pulsing Current)

From the top diagram of Fig. 7(b) and according to the theorem of similar triangles

$$\frac{1-H}{H}=\frac{\theta}{\pi-\theta} \text{ and } \frac{\theta}{T_1}=\frac{\frac{\theta}{\pi}}{u_a-(1-\frac{\theta}{\pi})}.$$

H and T_1 can be resolved from the above equations

$$H=1-\frac{\theta}{\pi} \tag{A-18}$$

$$T_1=\pi(u_a-1)+\theta. \tag{A-19}$$

Fig. 4(d) and (e) shows that the negative voltage pulse causes the circulating current to decrease and the positive voltage pulse causes it to increase, resulting in high-frequency trapeziform currents. Although Section III-A has considered the circulating current variation from t_1 to t_4, it neglects the instantaneous change during t_1 to t_3 and t_2 to t_4, which will be discussed here.

Both the effective time of the positive and negative voltage pulses are $\frac{\theta-T_1}{\omega_c}$, therefore the peak-to-peak value of the trapeziform current can be deduced by

$$h=\frac{U_d}{L_1+L_2}\cdot\Delta t=\frac{U_d(\theta-T_1)}{(L_1+L_2)\omega_c}=\frac{U_d\pi(1-u_a)}{(L_1+L_2)\omega_c} \tag{A-20}$$

where u_a is the expression for modulation signal mentioned in (2).

For simplification, the trapeziform current can be approximated by a square wave, which is shown by the shaded area in the bottom picture of Fig. 7(b). As the carrier frequency is much larger than the modulation signal frequency, the modulation signal value is assumed to be constant in a carrier period. By applying the Fourier transform to the trapeziform current

$$i_{c3}=\frac{a_0}{2}+\sum\nolimits_{n=1}^{\infty}(a_n\cos n\omega_c t+b_n\sin n\omega_c t) \tag{A-21}$$

where

$$\begin{cases} a_n=\frac{1}{\pi}\int_{-\pi}^{\pi}-h\cos(n\omega_c t)d(\omega_c t) \\ \quad=\frac{1}{\pi}\int_{-\pi}^{\pi}\frac{-U_d\pi(1-u_a)}{(L_1+L_2)w_c}\cos(n\omega_c t)d(\omega_c t) \quad (n=0,1,2,\ldots) \\ b_n=\frac{1}{\pi}\int_{-\pi}^{\pi}-h\sin(n\omega_c t)d(\omega_c t) \\ \quad=\frac{1}{\pi}\int_{-\pi}^{\pi}\frac{-U_d\pi(1-u_a)}{(L_1+L_2)\omega_c}\sin(n\omega_c t)d(\omega_c t) \quad (n=1,2,\ldots). \end{cases} \tag{A-22}$$

Therefore

$$\begin{aligned} a_0&=\frac{1}{\pi}\int_{-\pi}^{\pi}\frac{-U_d\pi(1-u_a)}{(L_1+L_2)\omega_c}d(\omega_c t) \\ &=\frac{-U_d}{(L_1+L_2)\omega_c}\cdot\left(\theta-u_a\Big|_{-\frac{\theta}{2}}^{\frac{\theta}{2}}\right)=\frac{-U_d\theta}{(L_1+L_2)\omega_c} \end{aligned} \tag{A-23}$$

$$\begin{aligned} a_n&=\frac{1}{\pi}\int_{-\pi}^{\pi}\frac{-U_d\pi(1-u_a)}{(L_1+L_2)\omega_c}\cos(n\omega_c t)d(\omega_c t) \\ &=\frac{-U_d}{(L_1+L_2)\omega_c}\cdot\frac{1}{n}\cdot\sin(n\omega_c t)\Big|_{-\frac{\theta}{2}}^{\frac{\theta}{2}} \\ &=\frac{-U_d}{(L_1+L_2)\omega_c}\frac{2}{n}\sin(\frac{n\theta}{2}) \quad (n=1,2,\ldots). \end{aligned} \tag{A-24}$$

That is

$$\begin{cases} a_0=\frac{-U_d\theta}{(L_1+L_2)\omega_c} \\ a_n=\frac{-U_d}{(L_1+L_2)\omega_c}\frac{2}{n}\sin(\frac{n\theta}{2}) \quad (n=1,2,\ldots) \\ b_n=0. \end{cases} \tag{A-25}$$

Comparing (A-25) with (31) shows that the characteristics of circulating current in Case II are different from Case I. In Case II, the amplitude of the circulating current is in direct proportion to the dc voltage U_d, and is in inverse proportion to the impedance of the circulating current path L_1+L_2 and the angular frequency of carrier ω_c. The amplitude of the carrier-frequency circulating current is in direct proportion to $\sin\frac{\theta}{2}$, which is different from Case I, where the amplitude of carrier frequency component is in direct proportion to θ.

REFERENCES

[1] M. H. Hedayati and V. John, "Integrated common-mode inductor design for parallel interleaved converters," *IET Power Electron.*, vol. 9, no. 10, pp. 2130–2138, Aug. 2016.

[2] J. Wang, N. C. P. Chang, X. Feng, and A. Monti, "Design of a generalized control algorithm for parallel inverters for smooth microgrid transition operation," *IEEE Trans. Ind. Electron.*, vol. 62, no. 8, pp. 4900–4914, Aug. 2015.

[3] J. S. Siva Prasad, R. Ghosh, and G. Narayanan, "Common-Mode injection PWM for parallel converters," *IEEE Trans. Ind. Electron.*, vol. 62, no. 2, pp. 789–794, Feb. 2015.

[4] J. M. Guerrero *et al.*, "Output impedance design of parallel-connected UPS inverters with wireless load-sharing control," *IEEE Trans. Ind. Electron.*, vol. 52, no. 4, pp. 1126–1135, Aug. 2005.

[5] S. Augustine, M. K. Mishra, and N. Lakshminarasamma, "Adaptive droop control strategy for load sharing and circulating current minimization in low-voltage standalone DC microgrid," *IEEE Trans. Sustain. Energy*, vol. 6, no. 1, pp. 132–141, Jan. 2015.

[6] H. Cai, R. Zhao, and H. Yang, "Study on ideal operation status of parallel inverters," *IEEE Trans. Power Electron.*, vol. 23, no. 6, pp. 2964–2969, Nov. 2008.

[7] Z. Ye, D. Boroyevich, J. Choi, and F. C. Lee, "Control of circulating current in two parallel Three-Phase boost rectifier," *IEEE Trans. Power Electron.*, vol. 17, no. 5, pp. 609–615, Sep. 2002.

[8] C. T. Pan and Y. H. Liao, "Modeling and coordinate control of circulating currents for parallel Three-Phase Boost rectifiers with different load sharing," *IEEE Trans. Ind. Electron.*, vol. 55, no. 7, pp. 2776–2785, Jul. 2008.

[9] C. Yang and K. M. Smedley, "One-cycle-controlled three-phase grid-connected inverters and their parallel operation," *IEEE Trans. Ind. Appl.*, vol. 44, no. 2, pp. 663–671, Mar. 2008.

[10] M. H. Ravanji *et al.*, "Modeling and control of Zero-Sequence circulating current in parallel converters with space vector modulation," *IEEE J. Emerg. Sel. Topics Power Electron.*, vol. 5, no. 1, pp. 363–377, Mar. 2017.

[11] R. Ramos, D. Biel, E. Fossas, and F. Guinjoan, "Interleaving quasi sliding-mode control of parallel-connected buck-based inverters," *IEEE Trans. Ind. Electron.*, vol. 55, no. 11, pp. 3865–3873, Nov. 2008.
[12] F. Wang, Y. Wang, Q. Gao, C. Wang, and Y. liu, "A control strategy for suppressing circulating currents in parallel-connected PMSM drives with individual dc links," *IEEE Trans. Power Electron.*, vol. 31, no. 2, pp. 1680–1691, Feb. 2016.
[13] R. Simanjorang, Y. Miura, T. Ise, S. Sugimoto, and H. Fujita, "Application of series type BTB converter for minimizing circulating current and balancing power transformers in loop distribution lines," in *Proc. IEEE Conf. Power Convers.*, Apr. 2007, pp. 997–1004.
[14] P. Zhang, G. Zhang, and H. Du, "Circulating current suppression of parallel photovoltaic Grid connected converters," *IEEE Trans. Circuits Syst. II: Express Briefs*, 2017, doi: 10.1109/TCSII.2017.2789215.
[15] T. P. Chen, "Circulating Zero-Sequence current control of parallel Three-Phase inverters," in *Proc. Inst. Elect. Eng. Elect. Power Appl.*, Mar. 2006, vol. 153, no. 2, pp. 282–288.
[16] C. Y. Jia and E. K. K. Sng, "A novel communication strategy for decentralized control of paralleled Multi-Inverter systems," *IEEE Trans. Power Electron.*, vol. 21, no. 1, pp. 148–156, Jan. 2006.
[17] H. Ming, H. Haibing, X. Yan, and H. Zhongyi, "Distributed control for AC motor drive inverters in parallel operation," *IEEE Trans. Ind. Electron.*, vol. 58, no. 12, pp. 5361–5370, Dec. 2011.
[18] B. Wei, J. M. Guerrero, C. V. Juan, and X. Guo, "A circulating-current suppression method for parallel-connected voltage-source inverters with common DC and AC buses," *IEEE Trans. Ind. Appl.*, vol. 53, no. 4, pp. 3758–3769, Aug. 2017.
[19] T.-F. Wu, Y.-K. Chen, and Y.-H. Huang, "3C strategy for inverters in parallel operation achieving an equal current distribution," *IEEE Trans. Ind. Electron.*, vol. 47, no. 2, pp. 273–281, Apr. 2000.
[20] X. Sun, Y.-S. Lee, and D. Xu, "Modeling, Analysis, and Implementation of Parallel Multi-Inverter Systems with Instantaneous Average-current-sharing Scheme," *IEEE Trans. Power Electron.*, vol. 18, no. 3, pp. 844–856, May 2003.
[21] H. Ma, Z. Lin, L. Dong, and Q. Guo, "Modeling and analysis of switching frequency circulating current in three-phase parallel inverters," in *Proc. IEEE 23rd Int. Symp. Ind. Electron.*, Jun. 2014, pp. 568–573.
[22] T. Itkonen, J. Luukko, and A. Sankala, "Modeling and analysis of the dead time effects in parallel PWM two level three phase voltage source inverters," *IEEE Trans. Ind. Electron.*, vol. 24, no. 11, pp. 2446–2455, Nov. 2009.
[23] C.-C. Hou, "A multicarrier PWM for parallel three-phase active front-end converters," *IEEE Trans. Power Electron.*, vol. 28, no. 6, pp. 2753–2759, Jun. 2013.
[24] M. Narimani and G. Moschopoulos, "Three-Phase multimodule VSIs using SHE-PWM to reduce zero-sequence circulating current," *IEEE Trans. Ind. Electron.*, vol. 61, no. 4, pp. 1659–1668, Apr. 2014.
[25] J. S. S. Prasad, R. Ghosh, and G. Narayanan, "Common-Mode Injection PWM for Parallel Converters," *IEEE Trans. Ind. Electron.*, vol. 62, no. 2, pp. 789–794, Feb. 2015.
[26] W. Jiang *et al.*, "Suppression of zero sequence circulating current for parallel three-phase grid-connected converters using hybrid modulation strategy," *IEEE Trans. Ind. Electron.*, vol. 65, no. 4, pp. 3017–3026, Apr. 2018.
[27] T.-Po Chen, "Zero-Sequence circulating current reduction method for parallel HEPWM inverters between AC Bus and DC Bus," *IEEE Trans. Ind. Electron.*, vol. 59, no. 1, pp. 290–300, Jan. 2012.
[28] X. Zhang, W. Zhang, J. Chen, and D. Xu, "Deadbeat control strategy of circulating currents in parallel connection system of three-phase PWM converter," *IEEE Trans. Energy Convers.*, vol. 29, no. 2, pp. 406–417, Jun. 2014.
[29] X. Zhang *et al.*, "A coordinate control strategy for circulating current suppression in Multi-Parallel Three-Phase inverters," *IEEE Trans. Ind. Electron.*, vol. 64, no. 1, pp. 838–847, Jan. 2017.
[30] R. Zhu *et al.*, "Zero-Sequence voltage modulation strategy for Multi-Parallel converters circulating current suppression," *IEEE Trans. Ind. Electron.*, vol. 64, no. 3, pp. 1841–1852, Mar. 2017.
[31] J. Liu, H. Lin, and X. Qin, "Study on restraint of circulating current in parallel inverters system with SPWM modulation by adjusting phases of triangular carrier waves," in *Proc. 2nd Int. Symp. Instr. Meas., Sens. Netw. Autom.*, Dec. 2013, pp. 477–480.
[32] J. Liu, X. Qin, H. Lin, and L. Bu, "Analysis on Circulating Current of Parallel Inverter with SPWM Modulation for AC Motor Drive," in *Proc. Int. Conf. Model., Identification Control*, Jun. 2012, pp. 1080–1086.
[33] W. Jiang *et al.*, "Suppression of high frequency circulating current caused by asynchronous carriers for parallel there-phase grid-connected converters," *IEEE Trans. Ind. Electron.*, vol. 65, no. 2, pp. 1031–1040, Feb. 2018.
[34] J. Hu and H. Ma, "Synchronization of the carrier wave of parallel Three-Phase inverters with virtual oscillator control," *IEEE Trans. Power Electron.*, vol. 32, no. 10, pp. 7998–8007, Oct. 2003.

Authors' photographs and biographies not available at the time of publication.